New Approach Toward Nanosized Ferrous Ferric Oxide and Fe_3O_4-doped Titanium Dioxide Photocatalysts

Wing Sze Tung and Walid A. Daoud*

School of Applied Sciences and Engineering, Monash University, Churchill, VIC 3842, Australia

ABSTRACT In this article, ferrous ferric oxide and Fe_3O_4-doped titanium dioxide have been synthesized by a low-temperature sol−gel process. In particular, we studied the structural characteristics of newly synthesized photosensitive catalysts and their photocatalytic abilities under UV and visible light irradiation. The elemental composition, surface area, crystallinity, and morphology of synthesized catalysts were characterized by Fourier transformation infrared spectrophotometry, X-ray photoelectron spectroscopy, X-ray diffraction, and transmission electron microscopy with selected area electron diffraction and energy-dispersive X-ray spectroscopy. The UV−vis transmission, ζ-potential, and cytotoxicity of the synthesized catalysts are also discussed. It is anticipated that the synthesized ferrous ferric oxide arrays a prospective photocatalyst substitute for titanium dioxide.

KEYWORDS: Titanium dioxide • ferrous ferric oxide • sol−gel synthesis • doping • photocatalysis

INTRODUCTION

Purification from organic contamination is one of the most interesting challenges in catalysis today. Destruction of pollutants, organic contaminants, and hazardous microorganisms through advanced oxidation process using photosensitive semiconductors with the aid of solar light forms an emerging area of concurrent research, owing to their environmental-friendly benefits in the saving of resources such as water, energy, chemicals, and other cleaning materials (1−8).

Titanium dioxide nanostructures have consistently drawn much attention for their fascinating potential in environmental applications, such as self-cleaning, air/water purifications, water disinfection, hazardous waste remediation, sterilization, and deodorization (9−15). Although titanium dioxide has proven to be the most promising candidate among various photocatalysts (16−20), its use is limited due to its large photonic band gap (3.2 eV) and possible recombination of the generated electron−hole pairs by rapid charge-transfer process (21). Extensive research endeavors, therefore, have been devoted to develop heterogeneous photocatalysts with greater photocatalytic activities, by extending the effective absorption range of titanium dioxide from ultraviolet to visible region or by searching for new potential photosensitive catalysts as substitutes of titanium dioxide. Today, only few potential heterogeneous photocatalyst have been found (22), and some doped titanium dioxide catalysts have been reported (23−32).

Iron, one of the mostly used dopants, has been extensively investigated in boosting up the photocatalytic efficiency of titanium dioxide under visible light irradiation (33−37). Some researchers reported that, by creating a shallow trap in the titanium dioxide lattice because of its half-filled electronic configuration (38), iron-doped titanium dioxide shows high photocatalytic activities in visible light condition (400−800 nm) thanks to inhibiting electron/hole pair recombination in titanium dioxide and/or shifting the optical absorption range of titanium dioxide to lower energy (38). However, other researchers argued that there is no direct relationship between optical absorption features and photocatalytic behavior (37), and that iron ion doping decreases the photooxidation by acting as impurities in titanium dioxide (39, 40). Because of this controversy, the use of iron ion as a promising dopant remains controversial. Although the mechanism of narrowing the band gap and reducing the recombination rate of titanium dioxide with the aid of iron remain in the realm of debate (41−44), in general, it is believed that the photocatalytic behavior and efficiency are greatly affected by the type of iron dopant (i.e., Fe(II), Fe(III), or iron oxides), iron ion ratio, iron loading, and synthesis methods (38−40). Hence, further investigations are still required to explore iron as a doping catalyst through appropriate synthesis processes.

To the best of our knowledge, although iron, ferric oxide and ferrite oxide have been known as effective dopants for photocatalyst, ferrous ferric oxide has never been considered. In this paper, a systematic investigation in the synthesis of ferrous ferric oxide and ferrous ferric oxide-doped titanium dioxide nanostructured particles by a simple low temperature sol−gel process is reported. The structural and photocatalytic properties of the resulting materials were investigated. The results suggest that the synthesized ferrous ferric oxide arrays a prospective photocatalyst substitute for titanium dioxide.

* To whom correspondence should be addressed. E-mail: Walid.Daoud@sci.monash.edu.au. Telephone: + 61 3 990 26411. Fax: + 61 3 990 26738.
Received for review June 18, 2009 and accepted October 6, 2009

DOI: 10.1021/am900418q

EXPERIMENTAL SECTION

Sol−Gel Process. Titanium dioxide, ferrous ferric oxide, and iron-doped titanium dioxide colloids were prepared using the precursors, 97% titanium tetraisopropoxide (Sigma-Aldrich, Germany) and 98% iron(III) nitrate nonahydrate (Alfa Aesar, England) in aqueous acidic conditions.

In the preparation of ferrous ferric oxide sol, 37% hydrochloric acid (Rowe Scientific, Australia) was added to aqueous mixture of glacial acetic acid (Rowe Scientific, Australia) and iron(III) nitrate nonahydrate. The molar ratio of the precursor, acetic acid, and hydrochloric acid was 1:5:1. Titanium dioxide sol was prepared according to the above-described method using titanium tetraisopropoxide precursor.

Iron-doped titanium dioxide sols were synthesized in two different molar ratios (Fe/Ti = 1 and 0.5). A mixture of glacial acetic acid and titanium tetraisopropoxide was added into iron(III) nitrate nonahydrate, followed by addition of water and 37% hydrochloric acid.

All resulting mixtures were heated at 60 °C under vigorous stirring for 2 h. The solid powders were obtained after precipitating the formulations using sodium carbonate (Rowe Scientific, Australia), followed by rinsing with distilled water and drying in oven at 60 °C for 24 h. Titanium dioxide and ferrous ferric oxide formulations are termed TO and FO, respectively. Iron-doped titanium dioxides with titanium dioxide/iron ratio of 1:1 and 1:0.5 are termed TF1 and TF2, respectively.

Optical Absorption. The UV−vis transmission was acquired on a UV−vis spectrometer (Varian Cary 300, Varian Techtron Pty Ltd., Australia) in a wavelength range of 200−700 nm.

Fourier Transformation Infrared (FT-IR) Spectrophotometry. FT-IR spectra were recorded on Varian FTS 1000 FT-IR spectrophotometer (Scimitar Series, Varian Australia Pty Ltd., Australia) using KBr discs in the range of 400 to 4000 cm^{-1} at a resolution of 4 cm^{-1}.

Morphology and Crystallinity. The surface morphology, structure, and grain size of the samples were studied by means of transmission electron microscopy (TEM), selected area electron diffraction (SAED), and energy-dispersive X-ray spectroscopy (EDX) using a JEOL JEM-2010 (JEOL, Japan) equipped with X-ray analysis of elements with EDX detector, operating at 200 kV of accelerating voltage.

Information on the chemical states of the samples was obtained using X-ray photoelectron spectroscopy (XPS; SKL-12, Sengyang, China), modified with a VG CLAM 4 MCD electron energy analyzer. The pressure inside the ion-pumped sample analysis chamber was 8×10^{-8} Pa with a dual anode source from VG (type XR3E2) using nonmonochromatic Mg Kα X-ray radiation (1253.6 eV) at 10 kV and 15 mA.

The crystallinity of solid powder extracted from the synthesized colloids was studied by X-ray diffractometer (Bruker D8 Advance, Bruker AXS, Germany) in the region of $2\theta = 20-80°$ using detector scan mode and operating at 40 kV and 40 mA with 2.2 kW Cu anode long fine focus ceramic X-ray tube. The phase composition of the catalysts was identified by calculating the lattice spacing according to the Bragg equation as below

$$\text{Lattice Parameter } (d) = \lambda/2 \sin\theta \qquad (1)$$

ζ-Potential. The ζ-potential was determined on a ZetaPlus analyzer (Brookhaven Instruments Corp., USA) using electrophoretic light scattering and Laser Doppler Velocimetry techniques. The samples were mixed with 1 mM potassium chloride (KCl) in appropriate dilution for the measurement. Ten replicate analyses were performed and the results were expressed in millivolts as the mean values.

Cytotoxicity. Cytotoxicity test was conducted using a mouse embryonic fibroblast (cell line NIH 3T3), which is commonly found in human skin and other connective tissues. Test solutions containing synthesized catalysts were applied to the fibroblast cell line, where the cells were grown in Dulbecco's modified Eagle's medium (DMEM) supplemented with 10% new born calf serum with 100 U/m gentamycin. Exponentially growing cells were then dispersed for identifying the extent of cell decay induced by the test solutions. The cell counts reported are the average of triplicate runs.

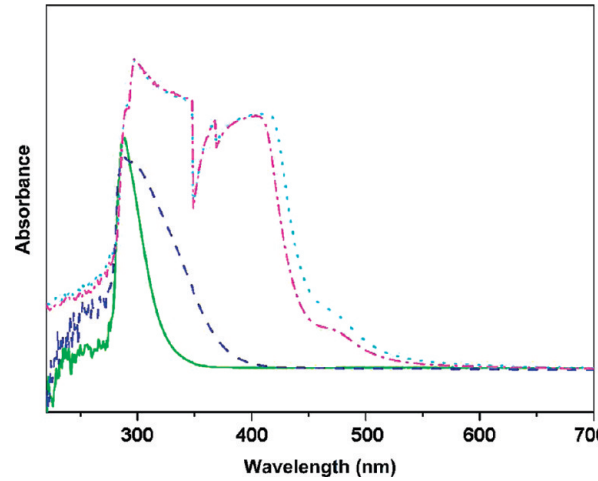

FIGURE 1. UV−vis transmission of TO (green solid line), FO (blue dashed line), TF1 (aqua dotted line) and TF2 (pink dash-dot line).

Photocatalytic Activity. The dynamic wet-state photocatalytic effectiveness was evaluated by examining the change of concentration of a colorant solution. 1.25×10^{-3} mol solid powder of synthesized catalysts were mixed with 50 mL acetic acid aqueous solution (5 mg/L, pH 1) of 3,7-bis(dimethylamino)phenazathionium chloride (methylene blue). The mixed colorant solutions were stored in dark condition for 1 h for the organic chemisorption on the surface of the catalysts. The oxide-containing colorant solution was vigorously shaken under UV irradiation (blacklight blue lamp, F18W/BLB-T8, Sylvania), operating at 18 W with 1.2−1.3 mW cm^{-2} irradiance, or visible light irradiation (cool white lamp, F18T8/840, Crompton), operating at 18 W with 0.19 mW cm^{-2} irradiance (UV intensity = 0.014 mW cm^{-2}). The spectral irradiance of the UV light sources is shown in Figure S1 in the Supporting Information. The UV−vis absorption spectra of the colorant solutions were recorded on Varian Cary 300 (Varian, Varian Techtron Pty Ltd., Australia), and the change of colorant concentration was analyzed following the intensity of the characteristic absorption peak of methylene blue at 655−664 nm.

Brunauer−Emmett−Teller (BET) Surface Area. The specific surface area of the catalysts was determined from nitrogen adsorption and desorption isotherms at 77 K using Micromeritics ASAP 2020 surface area and porosity analyzer (Micromeritics Instrument Corporation, U.S.A.). Prior to BET measurement, all catalysts (1 g) were degassed with nitrogen at 120 °C under vacuum for 10 h and backfilled with helium gas to remove excessive moisture or adsorbed contaminants on the samples' surface. The obtained data were automatically calculated by the BET equation with the computer-aided system.

RESULTS AND DISCUSSION

Optical Absorption. UV−vis transmission spectra of titanium dioxide doped with iron are shown in Figure 1. The synthesized TO and FO displayed a cutoff at 365 and 419 nm, respectively. FO showed greater UV−vis absorbency than TO in both UV and visible light regions. It can be seen that the absorption range of titanium dioxide can be extended to visible light region by doping with iron. Doping

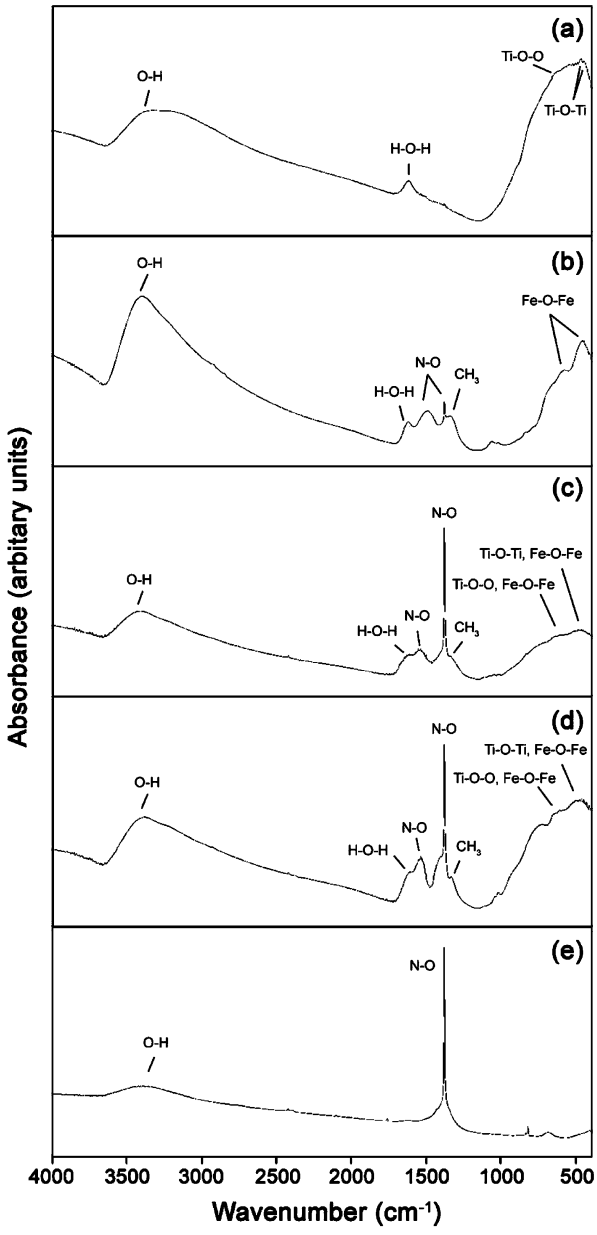

FIGURE 2. FI-IR spectra of (a) TO, (b) FO, (c) TF1, (d) TF2, and (e) FO precursor.

with iron effectively increased the absorption of TF1 and TF2 by showing new absorption cutoff at 642 and 614 nm, respectively. It is clear that the presence of iron greatly enhanced the light absorption in both UV and visible regions, wherein the absorption increased with increasing iron content. The improvement in absorption could be attributed to the charge transfer transition of interacting iron ion electrons within titanium dioxide band gap, and/or excitation of 3d electrons of iron to the titanium dioxide conduction band (45−47). Accordingly, it is anticipated that the photocatalytic efficiency of titanium dioxide would be significantly enhanced after doping with iron.

Fourier Transformation Infrared Spectrophotometry. FTIR spectroscopy was applied to identify the chemical structure of synthesized catalysts. Figure 2a,b shows the spectra of individual oxides (TO and FO). Figure 2c,d shows the spectra of doped oxides (TF1 and TF2). Figure 2e shows the spectra of iron oxide precursor. In the spectrum of TO, absorption bands were observed at 3327, 1624, 479, and 473 cm^{-1}. The absorption peak at 3327 cm^{-1} relates to the stretching vibration of hydroxyl groups, whereas the band at 1624 cm^{-1} is attributed to the bending vibration of H−OH groups and Ti−OH bond. In addition, the Ti−O−O bond was found at 650 cm^{-1} and the bands at 479 and 473 cm^{-1} were assigned to Ti−O−Ti bonds (48−50). In the spectrum of FO, the absorption bands observed at 3402 and 1625 cm^{-1} were ascribed to the stretching and bending vibrations of free or bonded OH and H−O−H hydroxyl groups respectively. The absorption peaks detected between 450 and 600 cm^{-1} were assigned to the stretching vibration of Fe−O−Fe in Fe_3O_4 (51). In addition, N−O stretching bands were identified at 1385 and 1496 cm^{-1}. These bands are probably attributed to nitrogen-containing byproduct generated during the synthesis process or due to the presence of a trace amount of unreacted iron(III) nitrate nonahydrate precursor. Referencing from TO and FO, the spectra of TF1 and TF2 showed the O−H stretching and H−O−H bending vibrations at ∼3400 and ∼1600 cm^{-1}, wherein the former is associated with basic hydroxyl groups and the latter corresponds to adsorbed molecular water (52). Similar to FO, N−O stretching bands were observed at ∼1550 and ∼1385 cm^{-1} in both TF1 and TF2; however, the intensity regarding N−O stretch was higher than FO indicating a possibility that more nitrogen-containing byproduct was generated or the presence of unreacted iron(III) nitrate nonahydrate precursor. The assignment of titanium dioxide and iron oxide were located in the region 450−650 cm^{-1}. Because of extensive overlap with the coordinated Ti−O−O, Ti−O−Ti, and Fe−O−Fe bonds in this region, corresponding bands could not be separately identified. On the other hand, the $-CH_3$ band observed at 1340−1342 cm^{-1} in Figure 2b−d could be attributed to acetic acid used in the formulation preparation process. Traces of acetic acid derivatives could only be completely removed by thermal treatment at elevated temperatures. However, this study aims at understanding the behavior of the photocatalysts synthesized at low temperature, thus it is expected that impurities may exist in the catalyst.

Morphology and Crystallinity. Transmission electron microscopy (TEM), energy-dispersive X-ray spectroscopy (EDX), X-ray photoelectron spectroscopy (XPS), and X-ray diffraction (XRD) were used to analyze the surface morphology, grain size, chemical composition, and crystallinity of synthesized catalysts.

The structure and grain size of titanium dioxide, iron oxide, and iron-doped titanium dioxide powders were observed by TEM as shown in Figure 3. The images exhibited that TO, FO, TF1, and TF2 consisted of agglomerates of primary particles with average grain size of 3.83, 2.95, 3.79, and 4.55 nm respectively, confirming that all synthesized catalysts are nanostructured. The grain size of doped titanium dioxide was apparently affected by the presence of iron. The crystal size decreased with increasing ratio of iron content, implying that the iron ions suppressed the growth

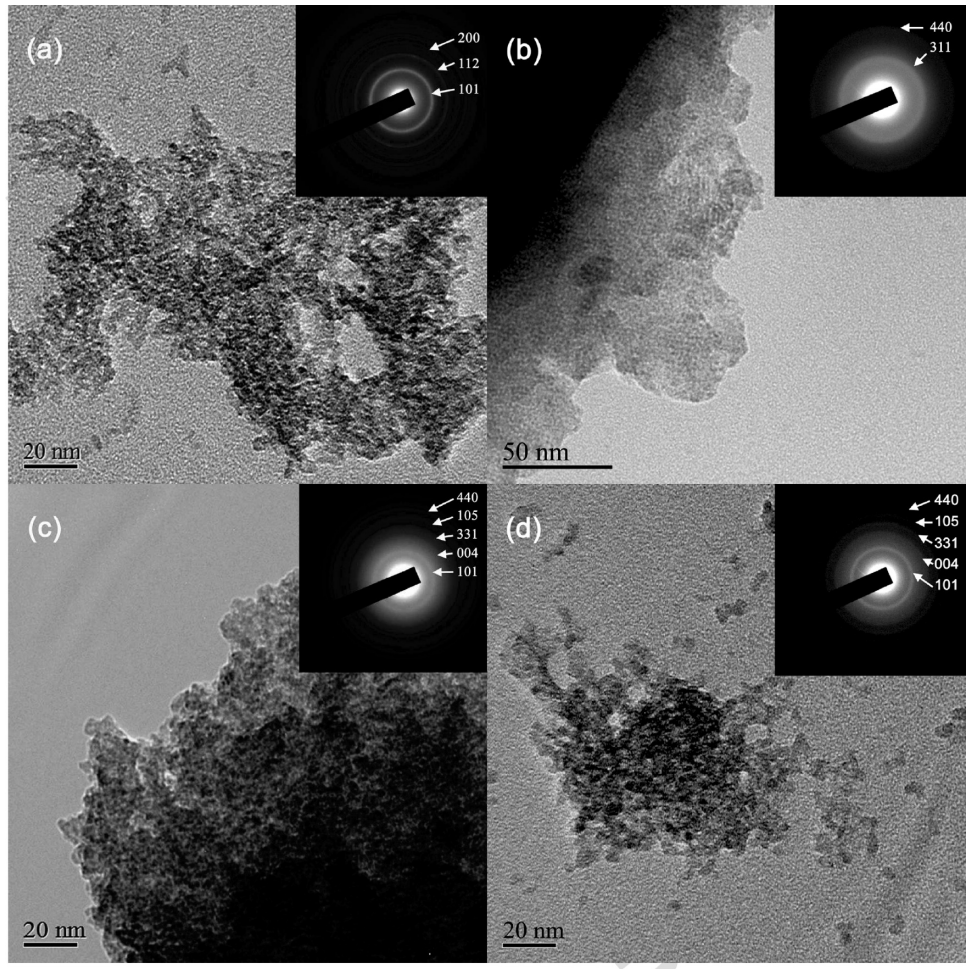

FIGURE 3. TEM images of (a) TO, (b) FO, (c) TF1, and (d) TF2.

of particles. The bright-field low resolution TEM micrographs were captured for verifying the chemical structure of the synthesized catalysts through identifying the crystallographic lattice spacing. After calculation, the TO's lattice spacing (Figure 3a) of 3.51, 2.33, and 1.89 nm were matched with that of the (101), (112), and (200) crystallographic planes of anatase titanium dioxide, and FO's lattice spacing (Figure 3b) of 2.53 and 1.48 nm were associated with that of the (311) and (440) crystallographic planes of iron(II, III) oxide (Fe_3O_4). For TF1 and TF2 (Figure 3c,d), the lattice spacing corresponded to that of the (101), (004), and (105) crystallographic planes of anatase titanium dioxide and (331) and (440) crystallographic planes of iron(II,III) oxide. These results are consistent with the FTIR analysis, confirming that TO and FO were of anatase and Iron(II,III) oxide form, respectively. It is also evident that the new oxide composites, TF1 and TF2, were successfully synthesized through the simple and low temperature chemical doping technique employed.

The elemental composition of synthesized catalysts was examined using EDX analysis. The EDX spectra are shown in Figure 4 and the corresponding atomic ratio is listed in Table 1. In agreement with the FTIR and TEM observations, iron(II,III) oxide and iron-doped titanium dioxide were evident as EDX results demonstrated that TO (Figure 4a) was composed of the elements of Ti and O; while FO (Figure 4b) was composed of the elements of Fe and O. Ti, Fe, and O were identified in TF1 (Figure 4c) and TF2 (Figure 4d). In TO, the approximate atomic ratio of 4:1 of O/Ti was similar to that in FO. Besides, the atomic ratio of O/Ti and O/Fe in TF1 and TF2 appeared to be consistent with that in TO and FO, which showed a 1:4 ratio of Ti/O. The measured atomic ratios are higher than the expected stoichiometric ratios of O/Ti and O/Fe, which are 2:1 and 4:3, respectively. The higher oxygen content could be attributed to the amorphous structure of the low-temperature synthesized catalysts as revealed by XRD analysis and/or to the presence of nitrogen-containing and coordinated acetic acid impurities as evident by FTIR. Comparing the Fe/Ti ratio between doped titanium dioxides, TF1 (synthesized with 1:1 molar ratio of titanium/iron oxide precursors) had an atomic ratio of 1:1 Fe/Ti, whereas TF2 (synthesized with 1:0.5 molar ratio of titanium/iron oxide precursors) had an atomic ratio of 0.5:1 Fe/Ti, confirming that the actual elemental composition of pure iron(II,III) oxide and iron-doped titanium dioxide is in line with the assumed nominal elemental composition.

To verify the EDX results, XPS surface analysis was used to quantify the amount of titanium and iron present in the near surface region of the oxides. Details of the XPS surface elemental composition of synthesized catalysts are shown in Table 2. All catalysts exhibited typical binding energies at the characteristic peaks of Ti(2p), Fe(2p) and O(1s) in the

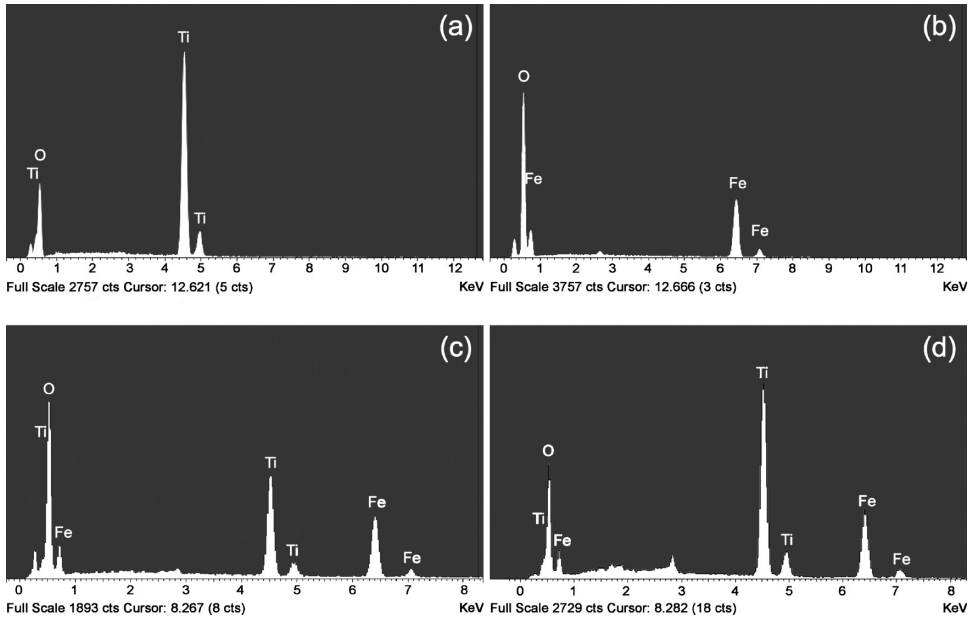

FIGURE 4. EDX spectra of (a) TO, (b) FO, (c) TF1, and (d) TF2.

Table 1. EDX of TO, FO, TF1 and TF2

	atomic %			atomic ratio			
sample	Ti	Fe	O	O/Ti	O/Fe	Fe/Ti	O/TiFe
TO	20.23		79.77	3.94			3.94
FO		21.84	78.16		3.58		3.58
TF1	9.71	10.22	80.07	8.25	7.83	1.05	4.02
TF2	12.69	6.36	80.95	6.38	12.73	0.50	4.25

region of 458.5, 530, and 711 eV, respectively (53). In all oxides, the amount of oxygen calculated from XPS data was slightly higher than that obtained from EDX, which showed a 1:5.5 ratio of titanium or iron to oxygen. However, the XPS data of the titanium-to-iron ratio of doped oxides was consistent with those of EDX data as well as with the assumed nominal ratio in which the elemental composition ratio of TF1 and TF2 (titanium/iron) were 1:1 and 1:0.5. Similar to EDX analysis, the relatively higher oxygen content might be due to the presence of nitrogen-containing and derivatives of acetic acid impurities and/or to the hydroxyl groups of the catalysts due to limited crystallization. Moreover, XPS usually measures the elemental composition of the substance surface up to 1−10 nm depth. Therefore, XPS could be regarded as a bulk technique due to the small particles size of the catalysts (3−5 nm). Nevertheless, the combined results from FTIR, XRD, TEM, EDX and XPS suggest that the synthesized catalysts were composed of iron(II,III) oxide and iron-doped titanium dioxide.

The phase composition and crystallinity of synthesized catalysts were examined by X-ray diffraction characterization. The XRD patterns of TO, FO, TF1, and TF2 are illustrated in Figure 5. Anatase with high crystallinity was the dominant phase in TO as evident by sharp diffraction peaks at the lattice parameters of 3.51 (101), 2.33 (112), 1.88 (200), 1.66 (211), 1.48 (204), 1.34 (220), and 1.26 (215). The lattice parameters of 2.96 (220), 2.52 (311), 2.09 (400), 1.71 (422), 1.60 (511), 1.48 (440), and 1.27 (533) were barely identified in the XRD spectrum of FO. The presence of weak diffraction peaks also suggested limited crystallization of FO. Although the XRD pattern of FO indicated a rather amorphous nature, the identified diffraction peaks are well indexed to the spinel phase of iron(II,III) oxide. On the other hand, the XRD spectra of TF1 and TF2 demonstrated the formation of both titanium dioxide and iron oxide without significant structural changes because both anatase and spine iron(II,III) oxide phases were traced at similar 2θ to those of TO and FO. Comparing doped titanium dioxide samples, the anatase characteristic peaks are of greater intensity with decreasing iron content, particularly in the (101) anatase lattice plane. Conversely, the spinel characteristic peaks associated with iron oxide are more evident at higher iron content, particular in the (220) lattice plane. Moreover, the anatase crystallinity was greatly reduced after doping, which may be attributed to the fine dispersion of iron in the titanium dioxide lattice restricting crystallite growth. The XRD analysis is thus supported by the results obtained from FTIR, TEM, EDX, and XPS studies.

Table 2. Surface Elemental Composition and XPS Binding Energies of TO, FO, TF1, and TF2

	chemical composition (%); in parentheses, binding energy (eV)			atomic ratio			
sample	Ti (2p)	Fe (2p)	O (1s)	O/Ti	O/Fe	Fe/Ti	O/TiFe
TO	15.65 (457.6)		84.3 (529.2)	5.38			5.38
FO		15.45 (711.1)	84.55 (531.2)		5.46		5.46
TF1	7.61 (460.4)	7.72 (707.5)	84.67 (527.8)	11.14	11.00	1.01	5.54
TF2	10.43 (458.0)	4.96 (710.6)	84.61 (529.8)	8.13	16.92	0.48	5.49

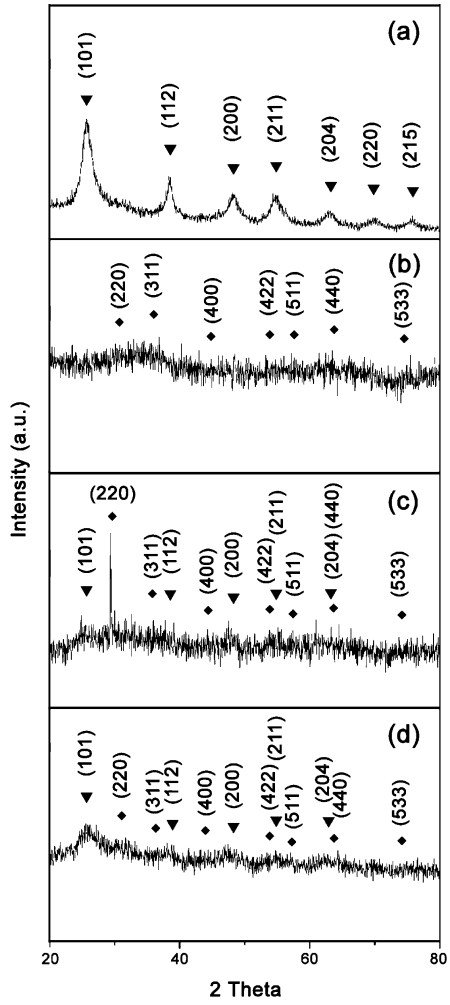

FIGURE 5. XRD pattern of solid powder (a) TO, (b) FO, (c) TF1, and (d) TF2.

Table 3. ζ-Potential of TO, FO, TF1, and TF2

	TO	FO	TF1	TF2
ζ-potential (mV)	27.45	49.98	27.26	24.91
standard deviation	2.11	4.61	1.88	2.58
pH value	2.12	1.59	1.70	1.92

ζ-Potential. ζ-potential was conducted to indicate the potential stability of synthesized colloidal dispersions. The results are listed in Table 3. The data displayed that all oxides have positive ζ-potentials, wherein FO showed the highest, followed by TO, TF1, and TF2. The most important factor affecting ζ-potential is pH; addition of an acid can lead to a buildup of positive charges. Accumulation of positive charges causes ζ-potential to be positive. Since all the oxides were synthesized under strong acidic condition (pH 1), they exhibited positive ζ-potential. In ζ-potential, a dividing line between stable and unstable dispersion is taken at ±30 mV. It was found that a good stability behavior was demonstrated in FO by showing 50 mV ζ-potential, which was even greater than that of TO. This indicates that the particles in the FO colloids are able to resist aggregation by repelling surrounding particles demonstrating practical usability. On the other hand, TO, TF1, and TF2 showed inferior instability due to the lower ζ-potential. This implies that the TO, TF1, and TF2 colloids are electrically unstable because the attraction between particles exceeds repulsion and that the colloidal particles tend to coagulate or flocculate. However, in view of practical application of suspensions of these catalysts, TO, TF1, and TF2 tend to coagulate and flocculate may be an obvious benefit rather than a drawback, when it comes to retrieve or remove the catalyst after use. Among iron-doped titanium dioxide, the oxide with higher iron content (Fe/Ti = 1 mol) showed better stability than that with lower iron content (Fe/Ti = 0.5 mol). With the support of grain size analysis from TEM, TF1 has smaller particle size than TF2. It is believed that the iron ions helped to stabilize the formed nanosized particles, thus preventing aggregation.

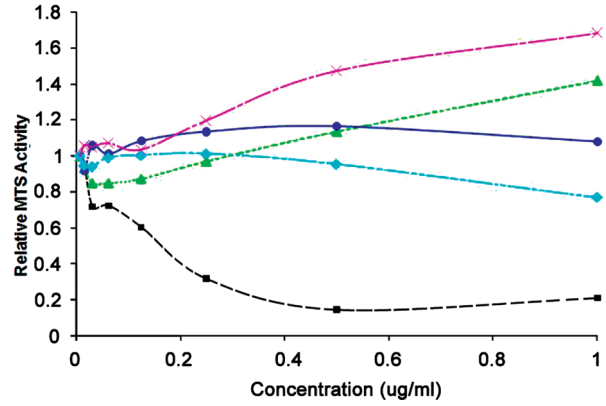

FIGURE 6. Cytotoxicity Evaluation of CDDP (---black square---), TO (···green triangle···), FO (—blue circle—), TF1 (—··aqua diamond—··) and TF2 (—· pink X—·).

Cytotoxicity. Cell proliferation was determined using MTS assay against a hormone-sensitive fibroblast cell line (NIH 3T3). A well-known anticancer drug, CDDP (Cisplatin), has been used as a positive control, and the cytotoxicity of synthesized catalysts was compared as illustrated in Figure 6. The relative MTS activity of all catalysts (TO, FO, TF1, TF2) had an insignificant drop when the appropriate-diluted catalyst-containing testing solution was first injected to the hormone-sensitive fibroblast cell line. This could be attributed to the change of the living environment for the fibroblast cells after being in contact with the synthesized particles, thus a variation of the relative MTS activity resulted during the first contact. Among all synthesized catalysts, the cell viability for both TO and TF2 increased with increasing concentration of test solution, indicating that anatase and iron-doped titanium dioxide (Fe/Ti = 0.5 mol) have no harmful effect on the tested mouse embryonic fibroblast cell. On the other hand, by increasing the concentration of FO and TF1 test solution in MTS assay, the amount of fibroblast cells decreased. Although FO and TF1 led to some reduction of relative MTS activity, the cell viability remained in the acceptable range since the relative MTS activity remained above 0.5. This signifies that the cells were still able to adapt and survive in the iron oxide and iron-doped titanium dioxide (Fe/Ti = 1 mol) testing solutions. The results suggest that the synthesized oxides do not have an effect on the viability of the fibroblast cell, implying a nonantiproliferative and noncytotoxic character.

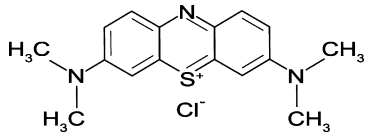

FIGURE 7. Molecular structure of methylene blue.

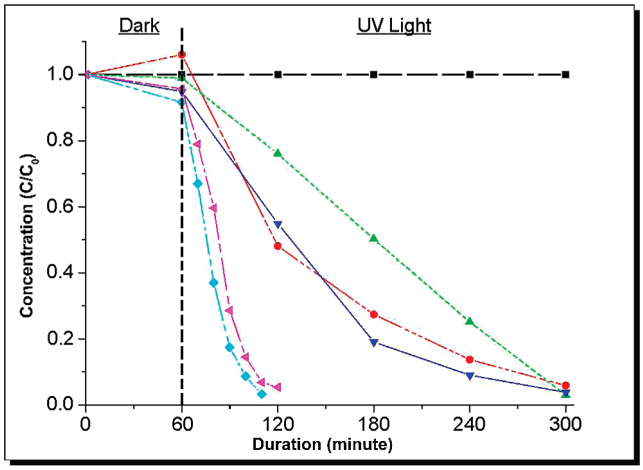

FIGURE 8. Decomposition of colorant under UV light: methylene blue solution (---black square---), P25 (—···red circle—···), TO (···green triangle up···), FO (—blue triangle down—), TF1 (—··aqua diamond—··) and TF2 (—·pink triangle left—·).

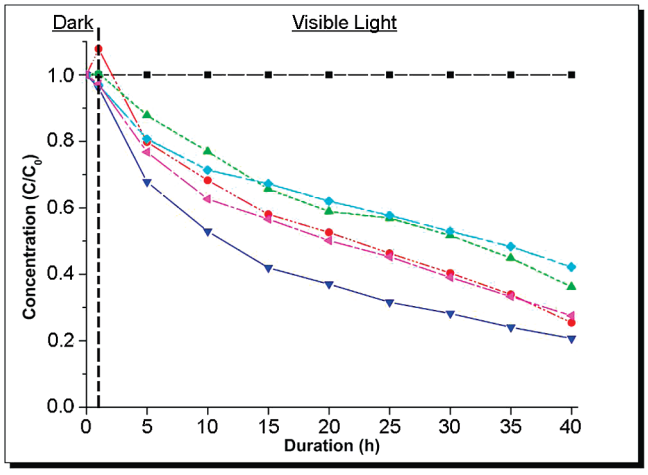

FIGURE 9. Decomposition of colorant under visible light: methylene blue solution (---black square---), P25 (—···red circle—···), TO (···green triangle up···), FO (—blue triangle down—), TF1 (—··aqua diamond—··) and TF2 (—·pink triangle left·).

Photocatalytic Activity. The photocatalytic activity was examined by a colorant decomposition test using methylene blue (Figure 7). The change in concentration of methylene blue pure solution and that in contact with different catalysts is demonstrated in Figures 8 and 9. Degussa P-25 (Degussa AG, Germany), labeled as P25, was used as received for comparison purpose in this experiment.

After exposure to UV irradiation, the concentration of pure methylene blue solution remained unchanged, whereas the concentration of all catalyst-containing methylene blue solutions decreased significantly. TF1 (Fe/Ti = 1 mol) showed the highest photocatalytic activity and was able to complete the colorant degradation process within 50 min, followed by TF2 (Fe/Ti = 0.5 mol), FO, P25, and TO which required 4 h to complete the degradation process. On the other hand, the catalysts performed differently under visible light irradiation. Similar to the results obtained under UV irradiation, the concentration of catalyst-containing methylene blue solution was greatly reduced, while that of pure methylene blue solution remained intact after exposure to visible light irradiation. However, when compared to the degradation rate under UV irradiation, the photoactivity of all catalysts considerably decreased under visible light irradiation, wherein all catalysts were unable to complete the decomposition process within 40 h. FO showed the highest photocatalytic property, followed by P25, TF2, TO, and TF1. While P25 and TF2 showed comparable colorant degradation rate, the activity of TO and TF1 was also similar. It is noteworthy to mention that under UV irradiation, TF1 and TF2 showed a significant enhancement in the photocatalytic activity, wherein iron-doped titanium dioxide was 4 times faster than pure titanium dioxide (TO) and pure iron(II,III) oxide (FO), and the commercial P25 catalyst. The improved photocatalytic activity may be attributed to the retardation of recombination of electron—hole pairs by introducing iron ions in the anatase lattice. Our finding is in good agreement with Zhu et al., who reported that the recombination rate can be decelerated by using iron ion as hole or electron traps in the titanium dioxide lattice, resulting in improvement of photocatalytic activity (54). In addition, to stabilize the photobleaching of methylene blue induced by visible light, acetic acid was added to the colorant solution. Araña et al. reported that the photocatalytic decomposition rate of dihydroxybenzenes can be modified using titanium dioxide in acetic acid (55), suggesting that the improved photoactivity may be correlated to the presence of acetic acid in the methylene blue solution. Nevertheless, the results also revealed that the photoacatalytic activity of doped titanium dioxide increased with increasing iron content, which is in disagreement with Hung et al., who stated that increasing doping level of iron ions can lead to reduction of photocatalytic activity in UV light condition as more recombination centers are created by the presence of iron species (36). The improved photocatalysis in presence of acetic acid was attributed the formation of additional $O_2^{\cdot -}$ radicals (55). These radicals may offset the slowdown of the photocatalytic activity caused by increasing iron content as found by Hung et al. (36) It is believed that not only titanium dioxide, iron oxide also reacted differently in the presence of acetic acid.

On the other hand, in visible light condition, the photocataltyic behavior of the catalysts changed. The results showed that pure iron(II,III) oxide possessed excellent photocatalytic property and outperformed P25. Besides, the photocatalytic activity of synthesized titanium dioxide (TO) can be made comparable to P25 after iron doping at 0.5 mol ratio (TF2); however, no photocatalytic enhancement was observed when iron doping was at 1 mol (TF1). From these results, it is believed that although the doping concentration played no adverse effect on the photocatalytic activity of doped titanium dioxide under UV light; the formation of recombination sites by the presence of iron ions had direct

Table 4. BET Surface Area of P25, TO, FO, TF1, and TF2

	P25	TO	FO	TF1	TF2
BET surface area (m^2/g)	70.23	282.64	90.33	212.98	229.80
single point surface area (m^2/g)	68.03	258.09	88.75	200.06	212.28

effect on the photoactivity of titanium dioxide in visible light condition (36). The findings indicate that the photocatalysts reacted differently according to the type of light irradiation. Hence, suitable photocatalysts have to be selected based on the particular application in order to achieve maximum photocatalytic function.

Besides, dissolution of iron was observed during the photocatalytic evaluation. Atomic absorption spectrometry has been conducted and the results are in agreement with Araña et al. (56−58) that the iron-containing catalysts release iron ions into the MB solution as shown in Table S1 in the Supporting Information. Given that a complete photocatalysis requires a complete degradation of acetic acid, which was presented at high concentration, it was not possible to establish whether iron ions return to the catalyst surface at the end of photocatalysis as previously reported (56−58).

BET Surface Area. Table 4 summarizes the BET surface area of synthesized catalysts. TO showed the largest BET surface area followed by TF2, TF1, FO, and P25. Among iron-doped titanium dioxides, the BET surface area decreased slightly by increasing the dopant concentration, indicating the presence of iron ion would lower the surface area of the catalyst. Although TO had the largest BET surface area (283 m^2/g), the photocatalytic ability under visible light was lower than P25 (70.23 m^2/g). Moreover, FO with surface area of 90 m^2/g exhibited the best photocatalytic performance. Iron-doped titanium dioxide with higher BET surface area (TF2) presented greater photocatalytic ability in the decomposition of methylene blue under visible light than that of TF1 with lower BET surface area. However, TF1 showed greater photocatalytic performance than TF2 in the decomposition of methylene blue under UV light irradiation. Although the surface area of catalysts is regarded as one of the most crucial factors in terms of photocatalytic efficiency, the results suggested that type of light irradiation plays a more important role than the surface areas in this study.

CONCLUSIONS

Nanosized noncytotoxic iron(II,III) oxide and Fe_3O_4-doped titanium dioxide were successfully synthesized in 2 h of preparation time using a simple low temperature sol−gel process. This process resulted in not only nucleation of iron(II,III) oxide but also introduction of iron dopant to titanium dioxide in a precise doping ratio. While Fe_3O_4-doped titanium dioxides showed greater photocataltytic activity than synthesized anatase titanium dioxide as well as Degussa P-25 under UV irradiation, iron(II,III) oxide showed greater decomposition rate than Degussa P-25 in both UV and visible light conditions. The obtained results demonstrate potential of iron(II,II) oxide and Fe_3O_4-doped titanium dioxides particularly in solar-driven purification systems.

Acknowledgment. This work was financially supported by the Monash Research Graduate School and School of Applied Sciences and Engineering at Monash University. The authors are grateful to the Materials Research Centre, Department of Applied Physics, Applied Biology and Chemical Technology and Institute of Textiles and Clothing at the Hong Kong Polytechnic University for the XRD, TEM, cytotoxicity, and ζ-potential studies. Thanks are also due to Centre for Surface Analysis and Research at Hong Kong Baptist University for their assistance in the XPS study and Dr. Yanlin Zhang for his help in the atomic absorption study.

Supporting Information Available: Spectral irradiation of light source, and experimental detail and result of atomic absorption spectrometry in measuring the iron release. This material is available free of charge via the Internet at http://pubs.acs.org.

REFERENCES AND NOTES

(1) Halliday, P. J.; Beszedits, S. *Can. Text. J.* **1986**, *103*, 78.
(2) Gupta, G. S.; Prasad, G.; Singh, V. N. *Water Res.* **1990**, *24*, 45.
(3) Ramakrishna, K. R.; Viraraghavan, T. *Water Sci. Technol.* **1997**, *36*, 189.
(4) Pagga, U.; Taeger, K. *Water Res.* **1994**, *28*, 1051.
(5) Hoffmann, M. R.; Martin, S. T.; Choi, W.; Bahnemann, D. W. *Chem. Rev.* **1995**, *95*, 69.
(6) Neppolian, B.; Sakthivel, S.; Palanichamy, M.; Arabindoo, B.; Murugasen, V. *Stud. Surf. Sci. Catal.* **1998**, *113*, 329.
(7) Thompson, T. L.; Yates, J. T. *Chem. Rev.* **2006**, *106*, 4428.
(8) Lv, K. L.; Xu, Y. M. *J. Phys. Chem. B* **2006**, *110*, 6204.
(9) Parkin, I. P.; Palgrave, R. G. *J. Mater. Chem.* **2005**, *15*, 1689.
(10) Kikuchi, Y.; Sunada, K.; Iyoda, T.; Hashimoto, K.; Fujishima, A. *J. Photochem. Photobiol., A* **1997**, *196*, 51.
(11) Sopyan, I.; Watanabe, M.; Murasawa, S.; Hashimoto, K.; Fujishima, A. *J. Electroanal. Chem.* **1996**, *415*, 183.
(12) Dong, Y.; Bai, Z.; Zhang, L.; Liu, R.; Zhu, T. *J. Appl. Polym. Sci.* **2006**, *99*, 286.
(13) Yu, H.; Lee, S. C.; Yu, J.; Ao, C. H. *J. Mol. Catal. A: Chem.* **2006**, *246*, 206.
(14) Jia, B. Y.; Duan, L. Y.; Ma, C. L.; Wang, C. M. *Chin. J. Chem.* **2007**, *25*, 553.
(15) Wang, S.; Hou, W.; Wei, L.; Jia, H.; Liu, X.; Xu, B. *Surf. Coat. Technol.* **2007**, *202*, 460.
(16) Yu, J. C.; Yu, J. G.; Ho, W. K.; Jiang, Z. T.; Zhang, L. Z. *Chem. Mater.* **2002**, *14*, 3808.
(17) Yu, J. G.; Xiong, J. F.; Cheng, B.; Yu, Y.; Wang, J. B. *J. Solid State Chem.* **2005**, *178*, 1968.
(18) Fujishima, A.; Rao, T. N.; Tryk, D. A. *J. Photochem. Photobiol., C* **2000**, *1*, 1.
(19) Fox, M. A.; Dulay, M. T. *Chem. Rev.* **1993**, *93*, 341.
(20) Hoffmann, M. R.; Martin, S. T.; Choi, W.; Bahnemann, D. W. *Chem. Rev.* **1995**, *95*, 69.
(21) Chatterjee, D.; Dasgupta, S. *J. Photochem. Photobiol., C* **2005**, *6*, 186.
(22) Khedr, M. H.; Abdel Halim, K. S.; Soliman, N. K. *Mater. Lett.* **2009**, *63*, 598.
(23) Lv, K.; Zuo, H.; Sun, J.; Deng, K.; Liu, S.; Li, X.; Wang, D. *J. Hazardous Mater.* **2009**, *161*, 396.
(24) Asahi, R.; Morikawa, T.; Ohwaki, T.; Aoki, K.; Taga, Y. *Science* **2001**, *293*, 269.
(25) Umebayashi, T.; Yamaki, T.; Itoh, H.; Asai, K. *Appl. Phys. Lett.* **2002**, *81*, 454.
(26) Khan, S. U. M.; Al-Shahry, M.; Ingler, W. B. *Science* **2002**, *297*, 2243.
(27) Hong, X.; Wang, Z.; Cai, W.; Lu, F.; Zhang, J.; Yang, Y.; Ma, N.; Liu, Y. *Chem. Mater.* **2005**, *17*, 1548.
(28) Luo, H.; Takata, T.; Lee, Y.; Zhao, J.; Domen, K.; Yan, Y. *Chem. Mater.* **2004**, *16*, 846.
(29) Dvoranova, D.; Brezova, V.; Mazur, M.; Malati, M. A. *Appl. Catal., B* **2002**, *37*, 91.
(30) Martin, S. T.; Morrison, C. L.; Hoffmann, M. R. *J. Phys. Chem.* **2004**, *98*, 13695.

(31) Li, X. Y.; Yue, P. L.; Kutal, C. *New J. Chem.* **2003**, *27*, 1264.
(32) Zuo, H. S.; Sun, J.; Deng, K. J.; Su, R.; Wei, F. Y.; Wang, D. Y. *Chem. Eng. Technol.* **2007**, *30*, 577.
(33) Vijayan, P.; Mahendiran, C.; Suresh, C.; Shanthi, K. *Catal. Today* **2009**, *141*, 220.
(34) Khan, R.; Kim, S. W.; Kim, T. J.; Nam, C. M. *Mater. Chem. Phys.* **2008**, *112*, 167.
(35) Adán, C.; Bahamonde, A.; Fernández-García, M.; Martínez-Arias, A. *Appl. Catal., B* **2007**, *72*, 11.
(36) Hung, W. C.; Fu, S. H.; Tseng, J. J.; Chu, H.; Ko, T. H. *Chemosphere* **2007**, *66*, 2142.
(37) Navío, J. A.; Colón, G.; Macías, M.; Real, C.; Litter, M. I. *Appl. Catal., A* **1999**, *177*, 111.
(38) Choi, W.; Termin, A.; Hoffmann, M. R. *J. Phys. Chem.* **1994**, *98*, 13669.
(39) Litter, M. I.; Navio, J. A. *J. Photochem. Photobiol., A* **1996**, *98*, 171.
(40) Serpone, N.; Lawless, D. *Langmuir* **1994**, *10*, 643.
(41) Litter, M.; Nav'ıo, J. *J. Photochem. Photobiol., A* **1996**, *98*, 171.
(42) Piera, E.; Tejedor-Tejedor, M. I.; Zorn, M. E.; Anderson, M. A. *Appl. Catal., B* **2003**, *46*, 671.
(43) Ranjit, K.; Viswanathan, B. *J. Photochem. Photobiol., A* **1997**, *108*, 79.
(44) Ikeda, S.; Sugiyama, N.; Murakami, S.; Kominami, H.; Kera, Y.; Noguchi, H.; Uosaki, K.; Torimoto, T.; Ohtani, B. *Phys. Chem. Chem. Phys.* **2003**, *5*, 778.
(45) Zhu, J.; Chen, F.; Zhang, J.; Chen, H.; Anpo, M. *J. Photochem. Photobiol., A* **2006**, *180*, 196.
(46) Umebayashi, T.; Yamaki, T.; Itoh, H.; Asai, K. *J. Phys. Chem. Sol.* **2002**, *63*, 1909.
(47) Li, X.; Yue, P. L.; Kutal, C. *New J. Chem.* **2003**, *27*, 1264.
(48) Urlaub, R.; Posset, U.; Thull, R. *J. Non-Cryst. Solid* **2000**, *265*, 276.
(49) Lopez, T.; Gomez, R.; Sanchez, E.; Tzompantzi, F.; Vera, L. *J. Sol-Gel Sci. Technol.* **2001**, *22*, 99.
(50) Chen, Y. F.; Lee, C. Y.; Yeng, M. Y.; Chiu, H. T. *J. Cryst. Growth* **2003**, *247*, 363.
(51) Hong, R. Y.; Pan, T. T.; Han, Y. P.; Li, H. Z.; Ding, J.; Han, S. J. *J. Magn. Magn. Mater.* **2007**, *310*, 37.
(52) Munuera, G.; Rives-Arnau, V.; Saucedo, A. *J. Chem. Soc., Faraday Trans. 1* **1979**, *75*, 736.
(53) Wangner, C. D., Riggs, W. M., Davis, L. E., Moulder, J. F., Muilenberg, G. E., Eds.; *Handbook of X-ray Photoelectron Spectroscopy*; Perkin-Elmer Corp.: Eden Prairie, Minnesota, 1979.
(54) Zhu, J.; Zheng, W.; Hea, B.; Zhang, J.; Anpo, M. *J. Mol. Catal., A* **2004**, *216*, 35.
(55) Araña, J.; Doña Rodríguez, J. M.; González Díaz, O.; Herrera Melián, J. A.; Fernández Rodríguez, C.; Pérez Peña, J. *Appl. Catal., A* **2006**, *299*, 274.
(56) Araña, J.; González Díaz, O.; Miranda Saracho, M.; Doña Rodríguez, J. M.; Herrera Melián, J. A.; Pérez Peña, J. *Appl. Catal., B* **2001**, *32*, 49.
(57) Araña, J.; González Díaz, O.; Miranda Saracho, M.; Doña Rodríguez, J. M.; Herrera Melián, J. A.; Pérez Peña, J. *Appl. Catal., B* **2002**, *36*, 113.
(58) Araña, J.; González Díaz, O.; Doña Rodríguez, J. M.; Herrera Melián, J. A.; Garriga i Cabo, C.; Pérez Peña, J.; Carmen Hidalgo, M.; Navío-Santos, J. A. *J. Mol. Catal., A* **2003**, *197*, 157.

AM900418Q